Revision 3

High pressure behavior of liebenbergite: the most incompressible olivine-structured silicate

Dongzhou Zhang[1,2], Yi Hu[3], Jingui Xu[4], Robert T. Downs[5], Julia E. Hammer[3], Przemyslaw K. Dera[1,3]

[1.] Hawaii Institute of Geophysics and Planetology, University of Hawaii at Manoa

[2.] GeoSoilEnviroCARS, University of Chicago

[3.] Department of Geology and Geophysics, University of Hawaii at Manoa

[4.] Institute of Geochemistry, Chinese Academy of Sciences

[5.] Department of Geosciences, University of Arizona

Corresponding author: Dongzhou Zhang (dzhang@hawaii.edu)

Abstract

Nickel is an abundant element in the bulk earth, and nickel-dominant olivine, liebenbergite, is the only igneous nickel-rich silicate found in nature. In this study, we used high-pressure single crystal diffraction to explore the compressional behavior of a synthetic liebenbergite sample up to 42.6 GPa at ambient temperature. Over the studied pressure range, the liebenbergite sample retains the orthorhombic P*bnm* structure, and no phase transition is observed. A 3rd order Birch-Murnaghan equation of state was used to fit the pressure behavior of the unit cell volume, lattice parameters, the polyhedral volume and the average bond length within each polyhedron. The best-fit bulk modulus K_{T0} = 163(3) GPa and its pressure derivative K_{T0}' = 4.5(3). We find that liebenbergite is the most incompressible olivine-group silicate reported thus far, and Ni^{2+} tends to increase the isothermal bulk modulus of both olivine- and spinel-structured silicates. Consequently, Ni-rich olivine has a higher density compared to Ni-poor olivine at the upper

mantle P-T conditions, however enrichment of Ni inmantle olivine is generally too low to make this density difference relevant for fractionation or buoyancy.

1. Introduction

Nickel is the most abundant of the minor elements in the bulk earth. It is less common than iron, oxygen, silicon and magnesium, which make up 94% of the atoms in earth, yet slightly more common than calcium and aluminum (Allegre et al., 2001; McDonough and Sun, 1995). A geochemical study of the distribution of nickel in the earth can constrain our understanding of the earth's evolution, for example, core segregation (Fischer et al., 2015; Ringwood, 1959; Siebert et al., 2012). Though one can't directly measure the composition of the earth's core, it is estimated that the core contains ~5 wt% nickel, and the core is the largest reservoir of this element (McDonough, 2014). This estimate is based on two premises: 1) the assumption that the abundance of nickel in the bulk earth is chondritic, and 2) the calibrated relationship between nickel concentration in mantle rocks and their MgO content (McDonough, 2014; McDonough and Sun, 1995; Palme and O'Neill, 2014). However, most of the research on the nickel concentration in mantle rocks has thus far focused on the shallow materials (Korenaga and Kelemen, 2000; Matzen et al., 2013; McDonough and Sun, 1995; Palme and O'Neill, 2014), and the partitioning coefficients of nickel between minerals and melts are strongly influenced by pressure (Fischer et al., 2015; Li and Agee, 1996; Matzen et al., 2013; Matzen et al., 2017; Pu p al., 2017; Siebert et al., 2012). Under certain geological settings, nickel could be enriched in mantle minerals without directly interacting with the earth's core (Ishimaru and Arai, 2008;

Matzen et al., 2013; Straub et al., 2008), so it is possible to have some nickel-rich reservoir in the deep part of the silicate mantle.

In order to quantify the possibility of deep reservoirs of Ni-rich silicates, one needs to understand the high pressure behavior of nickel-rich silicates. Systematic research on Ni-rich silicates is still lacking. From a mineralogical perspective, one can't assume that nickel behaves the same as iron in silicates. For example, there are no nickel endmembers of garnet and pyroxene (Back et al., 2017; Burns, 1973; Campbell, 1968; Gentile, 1960), while iron endmembers of garnet (almandine) and pyroxene (ferrosilite) both exist. Nickel is highly compatible with mantle peridotites (Griffin et al., 1989; Hart and Davis, 1978; Mysen, 1979; Palme and O'Neill, 2014). Geological surveys show that nickel tends to be enriched in olivine under natural conditions (Ishimaru and Arai, 2008; Straub et al., 2008), and liebenbergite, the nickel end-member of olivine (De Waal, 1973), is the only igneous nickel-rich silicate found in nature (Supplementary Table S1, Back et al., 2017). Considering the abundance of olivine in the mantle, studying the high pressure behavior of liebenbergite will provide insights into nickel-bearing silicates at deep earth conditions.

Studies, described below, were previously carried out to constrain the phase diagram and stability field of liebenbergite. At high pressures and temperatures (P > ~4 GPa, T > 700 °C), the olivine-structured liebenbergite transforms into a cubic spinel (Akaogi et al., 1982; Akimoto et al., 1965; Ringwood, 1962). At even higher pressures (P > 14 GPa, T > 1400 °C), the Ni_2SiO_4 spinel decomposes into bunsenite (NiO) and stishovite (SiO_2) (Liu, 1975). The pressure-volume equation of state and elasticity of Ni_2SiO_4 spinel have previously been reported (Bass et al., 1984; Finger et al., 1979; Hazen, 1993; Mao et al., 1969; Sato, 1977b). The elasticity of liebenbergite measured at ambient conditions by Brillouin spectroscopy has also been reported (Bass et al., 1984). One high pressure Raman study has been carried out on liebenbergite to 35 GPa, and a phase transition was observed around 30 GPa in non-hydrostatic pressure environment (no pressure medium), yet the transition was not observed when water was used as the pressure medium (Lin, 2001). Surprisingly, no compressional equation of state study has been carried out on liebenbergite. In this report, we present our experimental results on the compressional equation of state measurement of liebenbergite up to 42.6 GPa at room temperature.

2. Experiments

The liebenbergite sample measured in this study was synthesized using the flux method (Ozima, 1976). Electron microprobe analysis conducted on a Cameca SX100 instrument at the University of Arizona determined the chemical composition of the sample as $Ni_{2.009}Si_{0.995}O_4$. Raman spectrum in the range of 200-5500 cm^{-1} suggests that the sample is anhydrous. A 15 μm × 15 μm × 5 μm fragment of liebenbergite was mounted onto a polymer holder for room pressure measurement. Then, the same crystal was loaded into a 4-pin DAC with a ~ ±34° opening angle. Helium was used as the pressure medium (Rivers et al., 2008), and gold was used to calibrate the pressure of the sample (Fei et al., 2007). The diffraction data were collected at the experimental station 13-BM-C of the Advanced Photon Source, Argonne National Laboratory, and the experimental details were described previously (Zhang et al., 2016a; Zhang et al., 2017). The crystal structure refinements were carried out with the ATREX/RSV, SHELXL, Olex2 and

VESTA software packages (Dera et al., 2013; Dolomanov et al., 2009; Sheldrick, 2008; Momma and Izumi, 2008). We used isotropic atomic displacement parameters (U_{iso}) for all atoms. The crystal structure model of Lager and Meagher (1978) was used to initialize the refinement. The crystal structure of liebenbergite is illustrated in Supplementary Figure S1. Figures of merits of the refinements, unit cell parameters, atomic coordinates and displacement parameters, bond lengths, polyhedral volumes and distortions at different pressures are given in Table 1, Supplementary Tables S2 & S3 and the supplementary CIF file.

3. Data analysis

3.1 Liebenbergite, the most incompressible olivine-structured silicate

Throughout the investigated pressure range (1 bar – 42.6 GPa), the liebenbergite sample retains the P*bnm* olivine structure. The compression curve of the liebenbergite sample does not show any abrupt changes, consistent with absence of structural transitions during compression. We fit the P-V compression curve of our sample with a 3rd order Birch-Murnaghan (BM3) equation of state (Figure 1) using the EoSFit7c software package (Angel et al., 2014). The best-fit parameters are: V_0 = 283.38(7) A^3, K_{T0} = 163(3) GPa, and K_{T0}' = 4.5(3). The K_{T0} of liebenbergite is significantly higher than K_{T0} of forsterite (Mg_2SiO_4, 123-136 GPa, Supplementary Table S4) and fayalite (Fe_2SiO_4, 125-136 GPa, Supplementary Table S4). The K_{T0} of liebenbergite is consistent with the adiabatic bulk modulus (K_{S0}) measured from Brillouin spectroscopy (165(2) GPa, Bass et al., 1984).

We also used the pressure-axial length BM3 equations of state to fit the lattice parameters *a, b* and *c* (Figure 2). The axial compressibilities were calculated from the best-fit linear moduli. The BM3 fitting was carried out with EoSFit 7c software (Angel et al., 2014). The best-fit BM3 parameters are listed in Table 2. The liebenbergite crystal shows elastic anisotropy on compression. At ambient pressure, the axial compressibilities of the three axes are: $\beta_a = 1.47(2)$ TPa^{-1}, $\beta_b = 2.63(2)$ TPa^{-1}, and $\beta_c = 2.14(1)$ TPa^{-1}. The ratio between the three axes using the BM3 fitting is $\beta_a:\beta_b:\beta_c = 1.00:1.79:1.46$. The **a**-axis is most incompressible, and the **b**-axis is the most compressible axis. The axial compressibility can also be calculated with the following equation:

$$\beta_i = \sum_j s_{ij} \qquad (1)$$

where s_{ij} is the elastic compliance of the mineral (Speziale et al., 2004). Using the adiabatic elastic compliances reported by (Bass et al., 1984), the axial compressibilities are calculated as: $\beta_a = 1.4(1)$ TPa^{-1}, $\beta_b = 2.5(1)$ TPa^{-1}, and $\beta_c = 2.2(1)$ TPa^{-1}. The axial compressibilities measured from our study are consistent with the results determined from Brillouin spectroscopy. The relative axial compressibility of liebenbergite is close to that of forsterite (Mg_2SiO_4, $\beta_a:\beta_b:\beta_c = 1.00:1.99:1.55$, Downs et al. (1996), $\beta_a:\beta_b:\beta_c = 1.0:2.2:1.6$, Finkelstein et al., 2014), fayalite (Fe_2SiO_4, $\beta_a:\beta_b:\beta_c = 1.00:2.44:1.30$, Zhang, 1998), tephroite (Mn_2SiO_4, $\beta_a:\beta_b:\beta_c = 1.00:2.40:1.36$, Zhang, 1998) and Co-olivine ($\beta_a:\beta_b:\beta_c = 1.00:2.26:1.61$, Zhang, 1998).

The isothermal bulk modulus of liebenbergite is 163(3) GPa, which is significantly higher than forsterite (Mg_2SiO_4, K_{0T} = 124-136 GPa), tephroite (Mn_2SiO_4, K_{0T} = 125.2 GPa), fayalite (Fe_2SiO_4, K_{0T} = 113-136 GPa), Co-olivine (K_{0T} = 144 GPa), monticellite ($CaMgSiO_4$,

K_{0T} = 113 GPa) and LiSc-olivine (K_{0T} = 118 GPa) (Supplementary Table S4 and Figure 3). The increase in the bulk modulus appears to be related to the compressibility of the **b**-axis, as reviewed above. An increase of Ni^{2+} in the olivine structure increases the isothermal bulk modulus. Similar to olivine, Ni-endmember of spinel also has a higher isothermal bulk modulus than the Mg-, Fe- and Co-endmembers of spinel (Figure 3). Previous Brillouin study has shown that liebenbergite has larger elastic moduli than other silicate olivines (Bass et al., 1984), which is consistent with our conclusion.

The large isothermal bulk modulus of liebenbergite is probably related to the small ionic radius of Ni^{2+}. Among all divalent cations, Ni^{2+} has the second smallest ionic radius, only larger than Be^{2+} (Shannon, 1976). Be^{2+} is too small to stay in the octahedral sites of olivine (Jollands et al., 2016), so Ni^{2+} is the smallest divalent cation that occupies the MO_6 octahedron in olivine. The bulk modulus is found to be related to the specific volume of a mineral. For an ionic crystal with Born power law repulsive potential, it can be proven mathematically that the product of bulk modulus (K) and the specific volume (V_0) of a mineral is a constant (Anderson and Anderson, 1970). The Anderson model is deduced from the harmonic approximation, so it is a first order approximation for closest-packed arrangement of ions (Anderson and Anderson, 1970), and olivine-structured mineral is known to have such closet-packed ionic arrangement (Thompson and Downs, 2001). Hazen and Finger (1979) established a similar relationship between polyhedral bulk modulus (K_p) and the polyhedral average bond length (d) in silicates and oxides as follows:

$$K_p d^3/Z_c = 7.5\pm0.2 \text{ Mbar}\cdot A^3 \qquad (2)$$

where Z_c is the cation formal charge. With this reasoning, the NiO_6 octahedron, with the smallest volume and the shortest average bond length, should be the most incompressible octahedron among all divalent cation MO_6 octahedra. It has been suggested that the compressibility of the olivine-structured silicate is dominantly controlled by the compressibility of the MO_6 octahedron (Bass et al., 1984), and therefore liebenbergite tends to be more incompressible than other olivine-structured silicates.

3.2 Compressional behavior of each polyhedron in liebenbergite

There are three filled polyhedral sites within the closest-packed array of oxygen atoms in liebenbergite, namely the Ni1 octahedron, the Ni2 octahedron and the Si tetrahedron. Our crystal structural refinement suggests that the Ni1 and Ni2 octahedra undertake most of the volumetric compression of the crystal, and Ni1 is more incompressible than Ni2 (Figure 4). The Si tetrahedron has a much smaller polyhedral volume and is significantly more incompressible than both NiO_6 octahedra (Figure 4). We fit the P-V compression curves of the three polyhedra with BM3 equation of state (Figure S2). The fits are weighted by the pressure and volumetric errors of the polyhedra, and the volumetric errors of the polyhedra are estimated using the following equation:

$$\delta V_i = 3\frac{\delta\langle a_i\rangle}{\langle a_i\rangle}V_i \qquad (3)$$

where V_i is the volume of each polyhedron, and $<a_i>$ is the average bond length of this polyhedron. The error of the average bond length of each polyhedron is calculated using the

Vesta software (Momma and Izumi, 2008). The best-fit parameters are listed in Table 2. In many silicates where Si tetrahedra form chains or frameworks, the volume of the Si tetrahedra stays almost constant during the initial compression, because most of the volume compression of the unit cell is accommodated by the rigid body tilting of the Si tetrahedra (e.g., Xu et al., 2017). The Si tetrahedral volume of liebenbergite decreases simultaneously as the compression begins, and we didn't observe a stagnant Si tetrahedral volume during the initial compression in liebenbergite. The non-stagnant tetrahedra has been observed in other neso-silicates, such as fayalite (Zhang et al., 2016b) and Ti-clinohumite (Qin et al., 2017), and it comes from the fact that Si tetrahedra are not connected in neso-silicates. The behavior of normalized average bond length is similar to the polyhedral volume (Figure S3). We fit the pressure vs. average bond length compression curves of the three polyhedra using BM3 equation of state (Table 2). Within the scattering of our data, we did not find any abrupt change in either the polyhedral volume or the average bond length. Bond valence is a physical quantity that estimates the oxidation states of atoms (Brown et al., 2003, Bickmore et al., 2017). Bond valence is defined as:

$$V = \sum \exp(\frac{R_0 - R_i}{b}) \qquad (4)$$

where V is the bond valence, R_0 is a tabulated parameter expressing the ideal bond length between two given atoms (for Ni-O bond, R_0 = 1.675 Å, for Si-O bond, R_0 = 1.624 Å), R_i is the measured bond length, and b = 0.37 Å is an empirical constant (Brown et al., 2003). From the bond length data (Table S3), we calculated the bond valence of each cation (Table 1). The bond valences of cations all increase with pressure, indicating that the Ni-O and Si-O bonds are stronger at high pressures.

The distortion of different polyhedra can be described by two parameters, namely the distortion index and the bond angle variance. Distortion index (D) describes the average deviation of the cation-oxygen bond lengths from their mean (Baur, 1974; Momma and Izumi, 2008), and is defined as:

$$D = \frac{1}{n}\sum_{i=1}^{n}\frac{|l_i - l_{av}|}{l_{av}} \qquad (5)$$

where l_i is the distance from the central cation to the *i*th coordinating oxygen, and l_{av} is the average bond length. Figure S4 shows the evolution of distortion indices of different polyhedra with pressure. Within the scattering of the data, we didn't find any systematic change in the distortion indices of the two octahedra, yet the distortion index of the Si-tetrahedron increases with pressure. The distortion index of the Ni1 site is always lower than that of the Ni2 site, which is consistent with previous observations that the M1 site in olivine is less distorted in interatomic distances (Birle et al., 1968).

For polyhedra with a regular shape, i.e., octahedra and tetrahedra, the deviation from the ideal polyhedral shape can be described by the bond angle variance (σ^2) (Momma and Izumi, 2008; Robinson et al., 1971). σ^2 is defined as:

$$\sigma^2 = \frac{1}{m-1}\sum_{i=1}^{m}(\phi_i - \phi_0)^2 \qquad (6)$$

where m is the number of O-M-O or O-T-O bond angles (3/2 times of the number of faces in the polyhedron), ϕ_i is the *i*th bond angle, and ϕ_0 is the ideal bond angle for a perfect regular polyhedron. For perfect regular polyhedra, $\sigma^2 = 0$. We calculate the σ^2 of the octahedra and the tetrahedra at different pressures (Figure S5, Table 1). In the investigated pressure range, the σ^2 of both octahedra systematically decrease, yet the σ^2 of the Si-tetrahedron increases with pressure. The σ^2 of the Ni1 site is always higher than that of the Ni2 site, which is consistent with previous observations that the M1 site in olivine is more distorted in bond angle than the M2 site (Birle et al., 1968). The pressure dependence of σ^2 indicates that the Ni1 and Ni2 octahedra become more regular in bond angle during compression, yet the Si tetrahedron becomes more and more irregular.

After assessing both the distortion index and the bond angle variance, we conclude that both the Ni1 and the Ni2 octahedra exhibit a trend towards an ideal octahedral shape at higher pressure. Similar behavior has been observed in the MgO_6 octahedra of forsterite up to 48 GPa (Finkelstein et al., 2014). Compared to the low transition pressure between olivine- and spinel-structured Ni_2SiO_4 (2-4 GPa, Liu, 1975), it is known that Mg^{2+} shifts the olivine transition pressure to ~13 GPa, and Mg-rich olivine is the dominant phase in the earth's upper mantle (Frost, 2008). The solid solution of liebenbergite in Mg-rich olivine is more relevant to the earth's upper mantle. Ni^{2+} is more compatible with olivine than with melt at the mantle conditions (Matzen et al., 2013; Matzen et al., 2017; Pu et al., 2017). Burns (1973) concludes that Ni^{2+} has relatively high crystal field stabilization energy in octahedral coordination, and therefore the octahedral sites in silicate solids are more favorable to accommodate Ni^{2+}, i.e., with a large equilibrium partitioning coefficient over silicate melt.

4. Implications

Olivine is the most abundant mineral in the earth's upper mantle. The concentration of Ni in upper mantle olivine is rather constant at different occurrences (about 0.4 wt% NiO at Fo# (100×Mg/[Mg+Fe]) ≈ 90, Ishimaru and Arai, 2008; Sato, 1977a). However, under certain geological settings, Ni concentration in olivine can be significantly higher than 0.4 wt%. Ni is found to be enriched in the olivine phenocrysts of the Hawaiian tholeiitic lava (0.25 - 0.60 wt% NiO, Lynn et al. 2017), and the origin for the Ni enrichment in Hawaiian olivine phenocryst is still under debate. It is possible that pryoxenite melting in the magma source leads to the Ni enrichment in the olivine phenocryst (Herzberg, 2006; Herzberg et al., 2016; Sobolev et al., 2007), while other researchers argue that the melting of periodotite at elevated pressure-temperature conditions could also generate olivine with enriched Ni (Matzen et al., 2013; Putirka et al., 2011). Besides Hawaii hotspot, Ni-rich olivine with NiO content up to 5 wt% has been found in a peridotite xenolith from the Kamchatka volcanic arc in Russia, which is likely due to the diffusion from Ni-rich sulfide melt (Ishimaru and Arai, 2008). Natural olivine with the highest Ni concentration ($Ni_{1.52}Mg_{0.33}Co_{0.05}Fe_{0.12}Si_{0.99}O_4$) has been found in the Barberton impact crater in South Africa, and it originates from a Ni-rich meteorite impact event (De Waal, 1973).

Except for the rare meteorite impact events, most Ni-rich olivine is associated with volcanoes. Previous study has suggested that mantle magma accumulation can occur as deep as 100 km (Clague, 1987), and melts in the mantle is olivine saturated for its entire journey to the surface (Herzberg, 1992). The density of Ni-rich olivine crystals at variable P-T conditions helps to estimate the force balance of olivine phenocryst crystallized in magma. We assess the density of olivine crystals with different compositions using the following approach. We use the parameterized isothermal equation of state from Angel et al., (2018) to calculate the density of olivine at different P-T conditions.

$$P(V,T) = \frac{3}{2}\,K_T(T,0)\left[\left(\frac{V_{0T}}{V}\right)^{7/3} - \left(\frac{V_{0T}}{V}\right)^{5/3}\right] \times \left\{1 + \frac{3}{4}(K'_T(T,0) - 4)\left[\left(\frac{V_{0T}}{V}\right)^{2/3} - 1\right]\right\}$$

$$V(T) = V_0\left[1 - \delta_T + \delta_T\left(1 - \frac{({\delta_T}^2 - 1)}{\delta_T}A\right)^B\right]$$

$$A = \alpha_{V,0}\left(\frac{\theta_E}{\xi_0}\right)\left(\frac{1}{\exp(\theta_E/T) - 1} - \frac{1}{\exp(\theta_E/T_{ref}) - 1}\right)$$

$$B = \frac{1}{\delta_T^2 - 1} \tag{7}$$

$$\xi_0 = \frac{(\theta_E/T)^2 exp(\theta_E/T)}{(exp\left(\frac{\theta_E}{T}\right) - 1)^2}$$

$$K_T(T,0) = K_{T0}\left[\frac{V_0}{V(T)}\right]^{\delta_T}$$

$$K'_T(T,0) = K'_{T0}\left[\frac{V(T)}{V_0}\right]^{\delta'}$$

In the equations above, the parameter θ_E = 484 K is the characteristic Einstein temperature of olivine, δ_T = 5.77 is the Anderson-Gruneisen parameter, and δ' = -3.5 is a parameterized constant (Angel et al., 2018). In the calculation we focus on three minerals and their solid solutions: forsterite (Mg_2SiO_4), fayalite (Fe_2SiO_4) and liebenbergite. We calculated the densities of pure forsterite, $(Mg_{0.9}Fe_{0.1})_2SiO_4$, $(Mg_{0.895}Fe_{0.099}Ni_{0.006})_2SiO_4$ (0.6 wt% NiO), and $(Mg_{0.855}Fe_{0.095}Ni_{0.05})_2SiO_4$ (5 wt% NiO) as functions of the depth to 300 km. The pressure-density equation of state parameters for fosterite and fayalite (K_T, K_T' and V_0) are taken from Finkelstein et al. (2014) and Zhang et al. (2016), respectively. The unit cell volume of solid solution at zero-pressure (V_0) is treated as the Voigt average of the three endmembers, as room pressure measurement has suggested very little excess volume effect in the olivine solid solution

(Bostrom, 1987). The bulk modulus of the solid solution (K_{T0}) is treated as the Reuss average of the endmembers, which is a good estimate when the crystal is under hydrostatic stress (Angel et al., 2018). We fix the pressure derivative of bulk modulus at 300 K (K_T') as 4.51, which is the best-fit value for the olivine with a mantle composition (Angel et al., 2018) and is close enough to our best-fit K' value of liebenbergite (4.5). We use the upper mantle geotherm profile from Anderson (1982) to correct the thermal effects, and the pressure-depth relationship is adopted from the PREM model (Dziewonski and Anderson, 1981). The calculated density of olivine at different depths is illustrated in Figure 5. From our calculations, we conclude that adding Ni to olivine would increase the density of olivine at the upper mantle conditions. Compared to the typical mantle olivine whose chemical composition is $(Mg_{0.9}Fe_{0.1})_2SiO_4$, adding 1 % of liebenbergite would increase the density of $(Mg_{0.9}Fe_{0.1})_2SiO_4$ olivine by 0.4 %.

Acknowledgements

This work was performed at GeoSoilEnviroCARS (Sector 13), Partnership for Extreme Crystallography program (PX^2), Advanced Photon Source (APS), and Argonne National Laboratory. GeoSoilEnviroCARS is supported by the National Science Foundation-Earth Sciences (EAR-1634415) and Department of Energy-Geosciences (DE-FG02-94ER14466). PX^2 program and the COMPRES-GSECARS gas loading system are supported by COMPRES under NSF Cooperative Agreement EAR-1661511. Use of the Advanced Photon Source was supported by the US Department of Energy, Office of Science, Office of Basic Energy Sciences, under Contract No. DE-C02-6CH11357. Development of ATREX IDL software is supported under National Science Foundation Grant EAR-1440005. Use of the COMPRES-GSECARS gas loading system was supported by COMPRES and GSECARS. Participations of PD and YH in this project are supported by NSF Grant EAR-1722969. We acknowledge associate editor Dr. Oliver Tschauner and technical editor Dr. Ross Angel for handling the manuscript and giving helpful feedbacks, and the two anonymous reviewers for the constructive comments. DZ acknowledges Dr. X. Pu (University of Michigan) and Dr. Z. Jing (SUSTC) for helpful discussions. The experimental data (IUCr CIF format) in this manuscript can be found in the supporting information.

References

Agee, C.B., 1998. Crystal-liquid density inversions in terrestrial and lunar magmas. Physics of the Earth and Planetary Interiors, 107, 63-74.

Akaogi, M., Akimoto, S.I., Horioka, K., Takahashi, K.I., Horiuchi, H., 1982. The System $NiAl_2O_4$-Ni_2SiO_4 at High-Pressures and Temperatures - Spinelloids with Spinel-Related Structures. J Solid State Chem 44, 257-267.

Akimoto, S.-I., Fujisawa, H., Katsura, T., 1965. The olivine-spinel transition in Fe_2SiO_4 and Ni_2SiO_4. Journal of Geophysical Research 70, 1969-1977.

Albarè e, F., 2003. Geochemistry : an introduction. Cambridge University Press, Cambridge ; New York.

Allegre, C., Manhes, G., Lewin, E., 2001. Chemical composition of the Earth and the volatility control on planetary genetics. Earth Planet Sc Lett 185, 49-69.

Anderson, D.L. and Anderson, O.L., 1970, The Bulk Modulus-Volume Relationship for Oxides. Journal of Geophysical Research 75, 3494-3500.

Andrault, D., Bolfan-Casanova, N., Lo Nigro, G., Bouhifd, M.A., Garbarino, G., Mezouar, M., 2011. Solidus and liquidus profiles of chondritic mantle: Implication for melting of the Earth across its history. Earth Planet Sc Lett 304, 251-259.

Andrault, D., Bouhifd, M.A., Itie, J.P., Richet, P., 1995. Compression and Amorphization of $(Mg,Fe)_2SiO_4$ Olivines: an X-Ray-Diffraction Study up to 70 GPa. Phys Chem Miner 22, 99-107.

Armentrout, M., Kavner, A., 2011. High pressure, high temperature equation of state for Fe_2SiO_4 ringwoodite and implications for the Earth's transition zone. Geophysical Research Letters 38.

Angel, R.J., 2000. Equations of state. Rev Mineral Geochem 41, 35-59.

Angel, R.J., Gonzalez-Platas, J., Alvaro, M., 2014. EosFit7c and a Fortran module (library) for equation of state calculations. Z Kristallogr 229, 405-419.

Angel, R.J., Alvaro, M., Nestola, F. 2018. 40 years of mineral elasticity: a critical review and a new parameterisation of equations of state for mantle olivines and diamond inclusions. Physics and Chemistry of Minerals 45, 95-113.

Back, M., Birch, W.D., Bojar, H.-P., Carter, J., Ciriotti, M.E., Fourestier, J.d., Dolivo-Dobrovolsky, D., Downs, R.T., Grew, E.S., Fascio, L., Ferraris, C., Ferraris, G., Garcia, J., Godelitsas, A., Golden, J., Gault, R., Halenius, U., Hawthorne, F.C., Horváth, L., Husdal, T., Imark, C.R., Campo, J.L.J.d., Kampf, A.R., Keutsch, F., Kjellman, J., Kolitsch, U., Kostov, R.I., Krivovichev, V.G., Kruszewski, Ł., Lapaire, J., Larsen, L.M., Manecki, A., Florencia, M., Márquez-Zavalía, Martin, R.F., Martins, T., Mees, F., Menchetti, S., Mills, S.J., Nickolay, D., Oberti, R., Ostrooumov, M., Pedersen, R.E., Peters, G.A., Revheim, O., Ritte, A.P., Rousseau, M., Schorn, S., Schumer, B.N., Stanley, C.J., Starkey, R., Vandenberghe, L., Vighetto, I., Vignola, P., Wang, J., Weissman, J., Witzke, T., Zaharia, L., 2017. The New IMA List of Minerals. International Mineralogical Association.

Bass, J.D., Weidner, D.J., Hamaya, N., Ozima, M., Akimoto, S., 1984. Elasticity of the Olivine and Spinel Polymorphs of Ni_2SiO_4. Phys Chem Miner 10, 261-272.

Baur, W., 1974. The geometry of polyhedral distortions. Predictive relationships for the phosphate group. Acta Crystallographica Section B 30, 1195-1215.

Bickmore, B.R., Craven, O., Wander, M.C., Checketts, H., Whitmer, J., Shurtleff, C., Yeates, D., Ernstrom, K., Andros, C. and Thompson, H., 2017. Bond valence and bond energy. American Mineralogist, 102(4), 804-812.

Birle, J.D., Gibbs, G.V., Moore, P.B., Smith, J.V., 1968. Crystal Structures of Natural Olivines. American Mineralogist 53, 807-824.

Bostrom, D., 1987. Single-crystal X-ray diffraction studies of synthetic Ni-Mg olivine solid solutions. American Mineralogist 72, 965-972.

Brown, I. D., Klages, P., & Skowron, A. 2003. Influence of pressure on the lengths of chemical bonds. Acta Crystallographica Section B: Structural Science, 59(4), 439-448.

Burns, R.G., 1973. The partitioning of trace transition elements in crystal structures: a provocative review with applications to mantle geochemistry. Geochimica et Cosmochimica Acta 37, 2395-2403.

Campbell, F.E., Roeder, P., 1968. The Stability of Olivine and Pyroxene in the Ni-Mg-Si-O system. American Mineralogist 53, 257-268.

Clague, D.A., 1987. Hawaiian xenolith populations, magma supply rates, and development of magma chambers. Bulletin of Volcanology 49, 577-587.

De Waal, S.A., Calk, L. C., 1973. Nickel Minerals from Barberton, South Africa: VI. Liebenbergite, a Nickel Olivine. American Mineralogist 58, 733-735.

Dera, P., Zhuravlev, K., Prakapenka, V., Rivers, M.L., Finkelstein, G.J., Grubor-Urosevic, O., Tschauner, O., Clark, S.M., Downs, R.T., 2013. High pressure single-crystal micro X-ray diffraction analysis with GSE_ADA/RSV software. High Pressure Res 33, 466-484.

Dolomanov, O.V., Bourhis, L.J., Gildea, R.J., Howard, J.A.K., Puschmann, H., 2009. OLEX2: a complete structure solution, refinement and analysis program. J Appl Crystallogr 42, 339-341.

Downs, R.T., Zha, C.-S., Duffy, T.S., Finger, L.W., 1996. The equation of state of forsterite to 17.2 GPa and effects of pressure media. American Mineralogist 81, 51-55.

Dziewonski, A.M., Anderson, D.L., 1981. Preliminary reference Earth model. Phys Earth Planet In 25, 297-356.

Fei, Y., Ricolleau, A., Frank, M., Mibe, K., Shen, G., Prakapenka, V., 2007. Toward an internally consistent pressure scale. Proceedings of the National Academy of Sciences 104, 9182-9186.

Finger, L.W., Hazen, R.M., Yagi, T., 1979. Crystal structures and electron densities of nickel and iron silicate spinels at elevated temperature or pressure. American Mineralogist 64, 1002-1009.

Finkelstein, G.J., Dera, P.K., Jahn, S., Oganov, A.R., Holl, C.M., Meng, Y., Duffy, T.S., 2014. Phase transitions and equation of state of forsterite to 90 GPa from single-crystal X-ray diffraction and molecular modeling. American Mineralogist 99, 35-43.

Fischer, R.A., Nakajima, Y., Campbell, A.J., Frost, D.J., Harries, D., Langenhorst, F., Miyajima, N., Pollok, K., Rubie, D.C., 2015. High pressure metal–silicate partitioning of Ni, Co, V, Cr, Si, and O. Geochimica et Cosmochimica Acta 167, 177-194.

Frost, D.J., 2008. The Upper Mantle and Transition Zone. Elements 4, 171-176.

Gentile, A.L., Roy, R., 1960. Isomorphism and Crystalline Solubility in the Garnet Family. American Mineralogist 45, 701-711.

Gillet, P., Richet, P., Guyot, F., Fiquet, G., 1991. High-temperature thermodynamic properties of forsterite. Journal of Geophysical Research: Solid Earth 96, 11805-11816.

Griffin, W.L., Cousens, D.R., Ryan, C.G., Sie, S.H., Suter, G.F., 1989. Ni in Chrome Pyrope Garnets - a New Geothermometer. Contrib Mineral Petr 103, 199-202.

Hart, S.R., Davis, K.E., 1978. Nickel Partitioning between Olivine and Silicate Melt. Earth Planet Sc Lett 40, 203-219.

Hazen, R.M., 1976. Effects of temperature and pressure on the crystal structure of forsterite. American Mineralogist 61, 1280-1293.

Hazen, R.M., 1977. Effects of temperature and pressure on the crystal structure of ferromagnesian olivine. American Mineralogist 62, 286-295.

Hazen, R.M., 1993. Comparative Compressibilities of Silicate Spinels: Anomalous Behavior of (Mg, Fe)$_2$SiO$_4$. Science 259, 206-206.

Hazen, R.M., Downs, R.T., Finger, L.W., 1996. High-pressure crystal chemistry of $LiScSiO_4$: An olivine with nearly isotropic compression. American Mineralogist 81, 327-334.

Hazen, R.M., Downs, R.T., Finger, L.W., Ko, J., 1993. Crystal chemistry of ferromagnesian silicate spinels: evidence for Mg-Si disorder. American Mineralogist 78, 1320-1323

Hazen, R.M., Finger, L.W., 1982. Comparative crystal chemistry: temperature, pressure, composition, and the variation of crystal structure. Wiley, Chichester ; New York.

Hazen, R.M., Finger, L.W., 1979. Bulk Modulus-Volume Relationship for Cation-Anion Polyhedra. Journal of Geophysical Research 84(B12), 6723-6728.

Herzberg, C., 1992. Depth and degree of melting of komatiites. Journal of Geophysical Research 97(B4), 4521-4540.

Herzberg, C., 2006. Petrology and thermal structure of the Hawaiian plume from Mauna Kea volcano. Nature 444, 605-609.

Herzberg, C., Vidito, C., Starkey, N.A., 2016. Nickel-cobalt contents of olivine record origins of mantle peridotite and related rocks. Am Mineral 101, 1952-1966.

Ishimaru, S., Arai, S., 2008. Nickel enrichment in mantle olivine beneath a volcanic front. Contrib Mineral Petr 156, 119-131.

Jing, Z.C., Karato, S.I., 2011. A new approach to the equation of state of silicate melts: An application of the theory of hard sphere mixtures. Geochimica Et Cosmochimica Acta 75, 6780-6802.

Jollands, M.C., Burnham, A.D., O'Neill, H.S.C., Hermann, J., Qian, Q., 2016. Beryllium diffusion in olivine: A new tool to investigate timescales of magmatic processes. Earth Planet Sc Lett 450, 71-82.

Kroll, H., Kirfel, A., Heinemann, R., Barbier, B., 2012. Volume thermal expansion and related thermophysical parameters in the Mg,Fe olivine solid-solution series. Eur. J. Mineral, 24, 935-956.

Kroll, H., Kirfel, A., Heinemann, R., 2014. Axial thermal expansion and related thermophysical parameters in the Mg,Fe olivine solid-solution series. Eur. J. Mineral, 26, 607-621.

Korenaga, J., Kelemen, P.B., 2000. Major element heterogeneity in the mantle source of the North Atlantic igneous province. Earth Planet Sc Lett 184, 251-268.

Kudoh, Y., Takéuchi, Y., 1985. The crystal structure of forsterite Mg_2SiO_4 under high pressure up to 149 kb. Zeitschrift für Kristallographie-Crystalline Materials 171, 291-302.

Lager, G.A., Meagher, E.P., 1978. High-temperature structural study of six olivines. American Mineralogist 63, 365-377.

Lesher, C.E. and Spera, F.J., 2015.Thermodynamic and Transport Properties of Silicate Melts and Magma, In The Encyclopedia of Volcanoes (Second Edition), 113-141, edited by Haraldur Sigurdsson,, Academic Press, Amsterdam.

Li, J., Agee, C.B., 1996. Geochemistry of mantle-core differentiation at high pressure. Nature 381, 686-689.

Lin, C.C., 2001. High-pressure Raman spectroscopic study of Co- and Ni-olivines. Phys Chem Minerals 28, 249-257.

Liu, L.G., 1975. Disproportionation of Ni_2SiO_4 to Stishovite Plus Bunsenite at High-Pressures and Temperatures. Earth Planet Sc Lett 24, 357-362.

Liu, L., Bassett, W.A., Takahashi, T., 1974. Isothermal compression of a spinel phase of Co_2SiO_4 and magnesian ilmenite. J. Geophys. Res 79, 1171-1174.

Liu, W., Li, B., 2006. Thermal equation of state of $(Mg_{0.9}Fe_{0.1})_2SiO_4$ olivine. Physics of the Earth and Planetary Interiors 157, 188-195.

Lynn, K.J., Shea, T., Garcia, M.O., 2017. Nickel variability in Hawaiian olivine: Evaluating the relative contributions from mantle and crustal processes. Am Mineral 102, 507-518.

Mao, H.-K., Takahashi, T., Bassett, W.A., 1970. Isothermal compression of the spinel phase of Ni_2SiO_4 up to 300 kilobars at room temperature. Physics of the Earth and Planetary Interiors 3, 51-53.

Mao, H.K., Takahashi, T., Bassett, W.A., Weaver, J.S., Akimoto, S.I., 1969. Effect of pressure and temperature on the molar volumes of wüstite and of three (Fe, $Mg)_2SiO_4$ spinel solid solutions. Journal of Geophysical Research 74, 1061-1069.

Mao, Z., Fan, D., Lin, J.-F., Yang, J., Tkachev, S.N., Zhuravlev, K., Prakapenka, V.B., 2015. Elasticity of single-crystal olivine at high pressures and temperatures. Earth Planet Sc Lett 426, 204-215.

Matzen, A.K., Baker, M.B., Beckett, J.R., Stolper, E.M., 2013. The Temperature and Pressure Dependence of Nickel Partitioning between Olivine and Silicate Melt. J Petrol 54, 2521-2545.

Matzen, A.K., Baker, M.B., Beckett, J.R., Wood, B.J., Stolper, E.M., 2017. The effect of liquid composition on the partitioning of Ni between olivine and silicate melt. Contrib Mineral Petr 172.

McDonough, W.F., 2014. Compositional Model for the Earth's Core, in: Turekian, K.K. (Ed.), Treatise on Geochemistry (Second Edition). Elsevier, Oxford, pp. 559-577.

McDonough, W.F., Sun, S.S., 1995. The Composition of the Earth. Chem Geol 120, 223-253.

Meng, Y., Fei, Y., Weidner, D.J., Gwanmesia, G.D., Hu, J., 1994. Hydrostatic compression of γ-Mg_2SiO_4 to mantle pressures and 700 K: Thermal equation of state and related thermoelastic properties. Phys Chem Miner 21, 407-412.

Mizukami, S., Ohtani, A., Kawai, N., Ito, E., 1975. High-pressure X-ray diffraction studies on β-and γ-Mg_2SiO_4. Physics of the Earth and Planetary Interiors 10, 177-182.

Momma, K., Izumi, F., 2008. VESTA: a three-dimensional visualization system for electronic and structural analysis. J Appl Crystallogr 41, 653-658.

Mysen, B.O., 1979. Nickel Partitioning between Olivine and Silicate Melt - Henrys Law Revisited. American Mineralogist 64, 1107-1114.

Nestola, F., Boffa Ballaran, T., Koch-Müller, M., Balic-Zunic, T., Taran, M., Olsen, L., Princivalle, F., Secco, L., Lundegaard, L., 2010. New accurate compression data for γ-Fe_2SiO_4. Physics of the Earth and Planetary Interiors 183, 421-425.

Nestola, F., Nimis, P., Ziberna, L., Longo, M., Marzoli, A., Harris, J.W., Manghnani, M.H., Fedortchouk, Y., 2011a. First crystal-structure determination of olivine in diamond: Composition and implications for provenance in the Earth's mantle. Earth Planet Sc Lett 305, 249-255.

Nestola, F., Pasqual, D., Smyth, J., Novella, D., Secco, L., Manghnani, M., Negro, A.D., 2011b. New accurate elastic parameters for the forsterite-fayalite solid solution. American Mineralogist 96, 1742-1747.

Ozima, M., 1976. Growth of nickel olivine single crystals by the flux method. Journal of Crystal Growth 33, 193-195.

Palme, H., O'Neill, H.S.C., 2014. Cosmochemical Estimates of Mantle Composition, in: Turekian, K.K. (Ed.), Treatise on Geochemistry (Second Edition). Elsevier, Oxford, pp. 1-39.

Poe, B.T., Romano, C., Nestola, F., Smyth, J.R., 2010. Electrical conductivity anisotropy of dry and hydrous olivine at 8 GPa. Physics of the Earth and Planetary Interiors 181, 103-111.

Pu, X., Lange, R.A., Moore, G., 2017. A comparison of olivine-melt thermometers based on D_{Mg} and D_{Ni}: The effects of melt composition, temperature, and pressure with applications to MORBs and hydrous arc basalts. American Mineralogist 102, 750-765.

Putirka, K., Ryerson, F.J., Perfit, M., Ridley, W.I., 2011. Mineralogy and Composition of the Oceanic Mantle. J Petrol 52, 279-313.

Qin, F., Wu, X., Zhang, D., Qin, S. and Jacobsen, S.D., 2017. Thermal Equation of State of Natural Ti-bearing Clinohumite. Journal of Geophysical Research: Solid Earth, 122(11), 8943-8951.

Ringwood, A.E., 1959. On the chemical evolution and densities of the planets. Geochimica et Cosmochimica Acta 15, 257-283.

Ringwood, A.E., 1962. Prediction and confirmation of olivine-spinel transition in Ni_2SiO_4. Geochimica et Cosmochimica Acta 26, 457-469.

Rivers, M., Prakapenka, V.B., Kubo, A., Pullins, C., Holl, C.M., Jacobsen, S.D., 2008. The COMPRES/GSECARS gas-loading system for diamond anvil cells at the Advanced Photon Source. High Pressure Res 28, 273-292.

Robinson, K., Gibbs, G.V., Ribbe, P.H., 1971. Quadratic Elongation: A Quantitative Measure of Distortion in Coordination Polyhedra. Science 172, 567-570.

Sato, H., 1977a. Nickel content of basaltic magmas: identification of primary magmas and a measure of the degree of olivine fractionation. Lithos 10, 113-120.

Sato, Y., 1977b. Equation of state of mantle minerals determined through high-pressure X-ray study. High Pressure Research: Applications in Geophysics, 307-312.

Shannon, R.D., 1976. Revised Effective Ionic-Radii and Systematic Studies of Interatomic Distances in Halides and Chalcogenides. Acta Crystallogr A 32, 751-767.

Sharp, Z.D., Hazen, R.M., Finger, L.W., 1987. High-Pressure Crystal-Chemistry of Monticellite, $CaMgSiO_4$. American Mineralogist 72, 748-755.

Sheldrick, G.M., 2008. A short history of SHELX. Acta Crystallogr A 64, 112-122.

Siebert, J., Badro, J., Antonangeli, D., Ryerson, F.J., 2012. Metal–silicate partitioning of Ni and Co in a deep magma ocean. Earth Planet Sc Lett 321–322, 189-197.

Smyth, J.R., Jacobsen, S.D., Hazen, R.M., 2000. Comparative Crystal Chemistry of Orthosilicate Minerals. Reviews in Mineralogy and Geochemistry 41, 187-209.

Sobolev, A.V., Hofmann, A.W., Kuzmin, D.V., Yaxley, G.M., Arndt, N.T., Chung, S.L., Danyushevsky, L.V., Elliott, T., Frey, F.A., Garcia, M.O., Gurenko, A.A., Kamenetsky, V.S., Kerr, A.C., Krivolutskaya, N.A., Matvienkov, V.V., Nikogosian, I.K., Rocholl, A., Sigurdsson, I.A., Sushchevskaya, N.M., Teklay, M., 2007. The amount of recycled crust in sources of mantle-derived melts. Science 316, 412-417.

Speziale, S., Duffy, T.S., Angel, R.J., 2004. Single-crystal elasticity of fayalite to 12 GPa. J Geophys Res-Sol Ea 109.

Straub, S.M., LaGatta, A.B., Pozzo, A.L.M.D., Langmuir, C.H., 2008. Evidence from high-Ni olivines for a hybridized peridotite/pyroxenite source for orogenic andesites from the central Mexican Volcanic Belt. Geochem Geophy Geosy 9, Q03007.

Thompson, R.M., and Downs, R.T. (2001) Quantifying distortion from ideal closest-packing in a crystal structure with analysis and application. Acta Crystallographica B57, 119-127.

Wilburn, D., Bassett, W., 1976. Isothermal compression of spinel (Fe_2SiO_4) up to 75 kbar under hydrostatic conditions. High Temp. High Pressures 8, 343-348.

Will, G., Hoffbauer, W., Hinze, E., Lauterjung, J., 1986. The compressibility of forsterite up to 300 kbar measured with synchrotron radiation. Physica B+C 139, 193-197.

Xu, J., Zhang, D., Dera, P. Zhang, B. and Fan, D., 2018, Experimental evidence for the survival of augite to transition zone depths, and implications for subduction zone dynamics. American Mineralogist, 102, 1516-1524.

Xu, J., Zhang, D., Fan, D., Zhang, J.S., Hu, Y., Guo, X., Dera, P. and Zhou, W., 2018. Phase Transitions in Orthoenstatite and Subduction Zone Dynamics: Effects of Water and Transition Metal Ions. Journal of Geophysical Research: Solid Earth, 123, B015169.

Zha, C.-S., Duffy, T.S., Downs, R.T., Mao, H.-K., Hemley, R.J., 1998. Brillouin scattering and X-ray diffraction of San Carlos olivine: direct pressure determination to 32 GPa. Earth Planet Sc Lett 159, 25-33.

Zhang, D.Z., Hu, Y., Dera, P.K., 2016a. Compressional behavior of omphacite to 47 GPa, Phys Chem Miner 43, 707-715.

Zhang, D.Z., Dera, P.K., Eng, P.J., Stubbs, J.E., Zhang, J.S., Prakapenka, V.B., Rivers, M.L., 2017. High Pressure Single Crystal Diffraction at PX^2. Jove-J Vis Exp, e54660.

Zhang, J.S., Hu, Y., Shelton, H., Kung, J., Dera, P., 2016b. Single-crystal X-ray diffraction study of Fe_2SiO_4 fayalite up to 31 GPa. Phys Chem Miner, 1-9.

Zhang, L., 1998. Single crystal hydrostatic compression of $(Mg,Mn,Fe,Co)_2SiO_4$ olivines. Phys Chem Miner 25, 308-312.

Table 1: Details of each polyhedron of liebenbergite at different pressures. The average bond length and the polyhedral volume are calculated by the Vesta software (Momma and Izumi, 2008). The bond valence is defined by Equation (4). The distortion index is defined by Equation (5). The bond angle variance is defined by Equation (6). The quadratic elongation is defined in Robinson et al., (1971), and has the same trend as the bond angle variance.

Table 2: Best-fit volumetric and linear BM3 parameters of the liebenbergite unit cell, its component polyhedra, lattice parameters and the average bond lengths of each polyhedron. BM3 fitting is carried out by the EoSFit7c software package (Angel et al., 2014).

Figure 1: Unit cell volume compression curve of liebenbergite and the best-fit BM3 pressure-volume equation of state. The error bars are smaller than the symbol. BM3 fitting is carried out by the EoSFit7c software package (Angel et al., 2014). Inset: the Eulerian strain-normalized pressure (f-F) plot. The linear trend of the f-F plot indicates that the BM3 fitting is suitable (Angel, 2000).

Figure 2: Normalized lattice parameters of liebenbergite as functions of pressure, with best-fit BM3 equations of states. BM3 fitting is carried out by the EoSFit7c software package (Angel et al., 2014).

Figure 3: Isothermal bulk moduli and their pressure derivatives of different olivine- and spinel-structured silicates. Solid symbols: olivine-structured silicates. Empty symbols: spinel-structured silicates. The 1σ confidence eclipse of K_{T0} and K_{T0}' of this study is shown as the dotted ellipse. Data and references can be found in Supplementary Table S4.

Figure 4: Normalized polyhedral volume compared to normalized unit cell volume at different pressures. The black dotted line is the Y = X identity line. The Ni1 and Ni2 octahedra shrink simultaneously with the unit cell, yet the Si tetrahedra shrink less than the unit cell volume at high pressures.

Figure 5: Calculated densities of olivines with different chemical compositions as functions of the depth in the upper mantle conditions. Green solid line: Mg_2SiO_4 (Fo100). Blue solid line: $(Mg_{0.9}Fe_{0.1})_2SiO_4$ (Fo90Fa10, typical upper mantle olivine composition). Red solid line: $(Mg_{0.895}Fe_{0.099}Ni_{0.006})_2SiO_4$ (0.6 wt% NiO, upper bound of NiO concentration in olivine phenocrysts of the Hawaiian tholeiitic lava, Lynn et al., 2017). Magenta solid line: $(Mg_{0.855}Fe_{0.095}Ni_{0.05})_2SiO_4$ (5 wt% NiO, upper bound of NiO concentration found in the peridotite xenolith from the Kamchatka volcanic arc in Russia, Ishimaru and Arai, 2008). Black dashed line: upper mantle density profile of the PREM model.

Table 1

Pressure (GPa)	0.0001	0.4(2)	3.9(3)	11.7(2)	20.0(1)	25.2(3)	31.4(2)	37.3(2)	42.6(5)
Ni1 Average bond length (A)	2.0803	2.0799	2.0637	2.0417	2.0185	2.0052	1.9838	1.9789	1.9655
Ni1 Polyhedral volume (A^3)	11.58(5)	11.55(13)	11.30(13)	10.98(15)	10.62(12)	10.42(14)	10.10(11)	10.04(15)	9.87(19)
Ni1 Distortion index	0.00882	0.00742	0.01431	0.00976	0.01221	0.00808	0.01057	0.00955	0.00496
Ni1 Quadratic elongation	1.0244	1.0255	1.0247	1.0226	1.0219	1.0212	1.0208	1.0191	1.017
Ni1 Bond angle variance	86.7801	90.8953	86.9672	79.9342	77.2471	75.1582	72.9187	66.9515	59.8429
Ni1 Effective coordination number	5.9822	5.9874	5.9474	5.9742	5.9652	5.9848	5.9654	5.9726	5.9941
Ni1 Bond valence	2.0071	2.0088	2.0950	2.1970	2.3125	2.3749	2.4997	2.5098	2.5775
Ni2 Average bond length (A)	2.1007	2.0982	2.0807	2.0498	2.0188	2.0021	1.9919	1.9732	1.9605
Ni2 Polyhedral volume (A^3)	12.00(6)	11.96(15)	11.67(15)	11.19(18)	10.74(14)	10.48(16)	10.33(13)	10.06(18)	9.89(19)
Ni2 Distortion index	0.02519	0.02692	0.02488	0.02643	0.02357	0.02488	0.02309	0.02553	0.02313
Ni2 Quadratic elongation	1.0209	1.0209	1.0198	1.0179	1.0152	1.0147	1.014	1.0128	1.0114
Ni2 Bond angle variance	72.374	71.9435	69.0663	61.6849	52.236	50.0929	48.1016	43.6025	38.3159
Ni2 Effective coordination number	5.8269	5.8053	5.8477	5.8188	5.8423	5.842	5.8602	5.8402	5.8558
Ni2 Bond valence	1.9232	1.9371	2.0135	2.1676	2.3281	2.4187	2.4602	2.5688	2.6397
Si Average bond length (A)	1.6417	1.6400	1.6357	1.6232	1.6152	1.6061	1.6019	1.5959	1.5974
Si Polyhedral volume (A^3)	2.23(1)	2.23(4)	2.21(4)	2.16(4)	2.12(3)	2.08(4)	2.06(3)	2.04(5)	2.04(6)
Si Distortion index	0.00632	0.00592	0.00583	0.00703	0.01173	0.007	0.01059	0.01243	0.01425
Si Quadratic elongation	1.0113	1.0112	1.0115	1.0122	1.0131	1.0136	1.0149	1.0137	1.0157
Si Bond angle variance	49.972	48.656	49.9954	53.8924	56.9767	60.1616	63.6643	58.4235	69.3632
Si Effective coordination number	3.989	3.9937	3.9946	3.9895	3.9784	3.9899	3.9838	3.9779	3.9635
Si Bond valence	3.8156	3.8305	3.8598	3.9518	4.0016	4.0704	4.0900	4.1171	4.0829

Table 2

Volumetric	V_0 (A^3)	K_{T0} (GPa)	K_{T0}’
Unit cell volume	283.38(7)	163(3)	4.5(3)
Ni1 octahedron	11.58(5)	191(11)	3.8(8)
Ni2 octahedron	11.99(5)	140(8)	4.8(8)
Si tetrahedron	2.23(1)	300(4)	8(4)
Axial	L_0 (A)	M_{T0} (GPa)	M_{T0}’
Lattice parameter *a*	4.72963(6)	682(7)	41(1)
Lattice parameter *b*	10.1256(8)	380(3)	10.6(2)
Lattice parameter *c*	5.9151(6)	468(2)	9.8(1)
<Ni1-O>	2.080(3)	5.6(3) $\times 10^2$	10(2)
<Ni2-O>	2.101(3)	4.0(2) $\times 10^2$	13(2)
<Si-O>	1.6419(3)	9(1)$\times 10^2$	32(16)

Figure 1

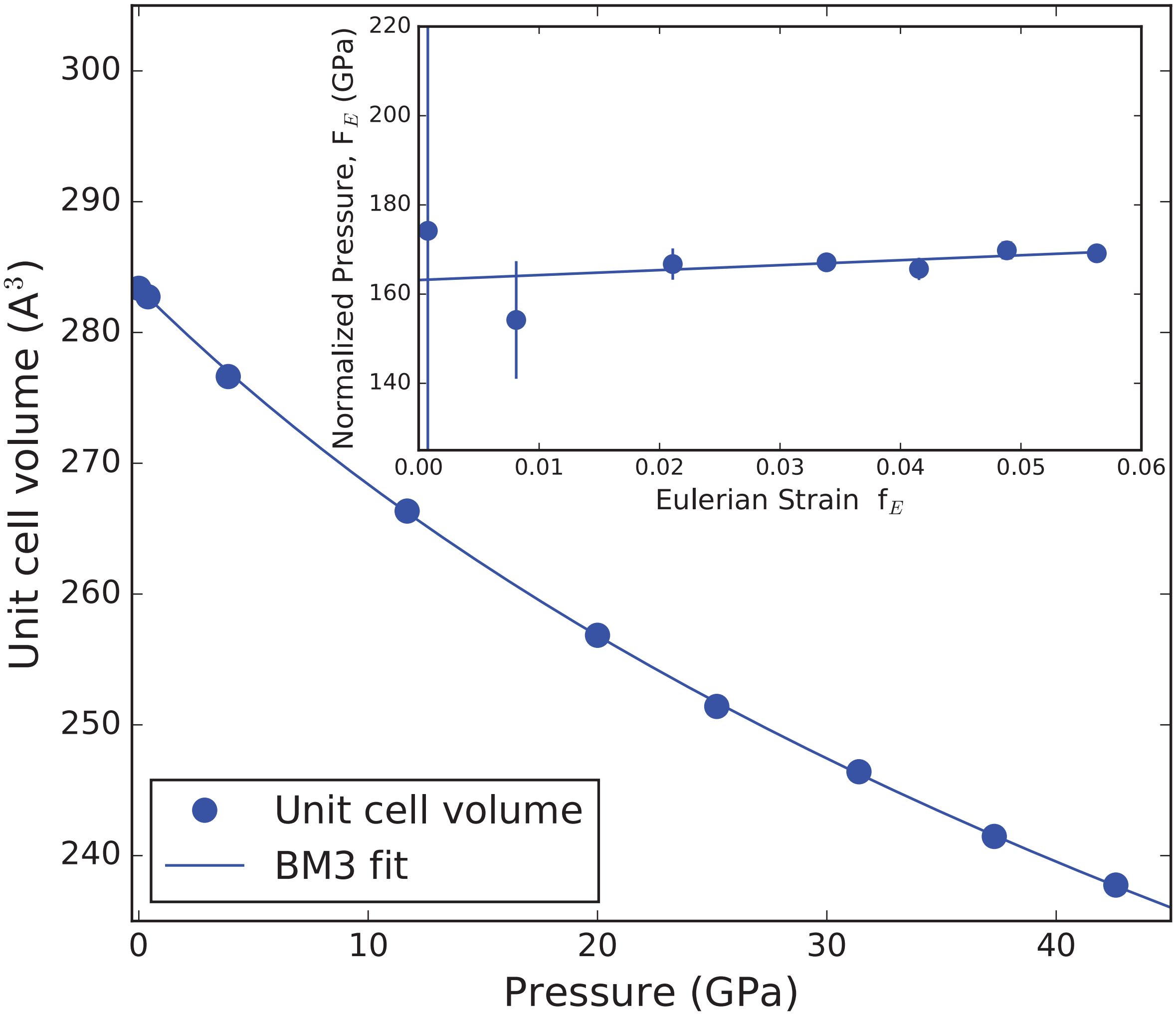
Unit cell volume (A^3)
300
290
280
270
260
250
240
0
10
20
30
40
Pressure (GPa)
Unit cell volume
BM3 fit
Normalized Pressure, F$_E$ (GPa)
220
200
180
160
140
0.00
0.01
0.02
0.03
0.04
0.05
0.06
Eulerian Strain f$_E$

Figure 2

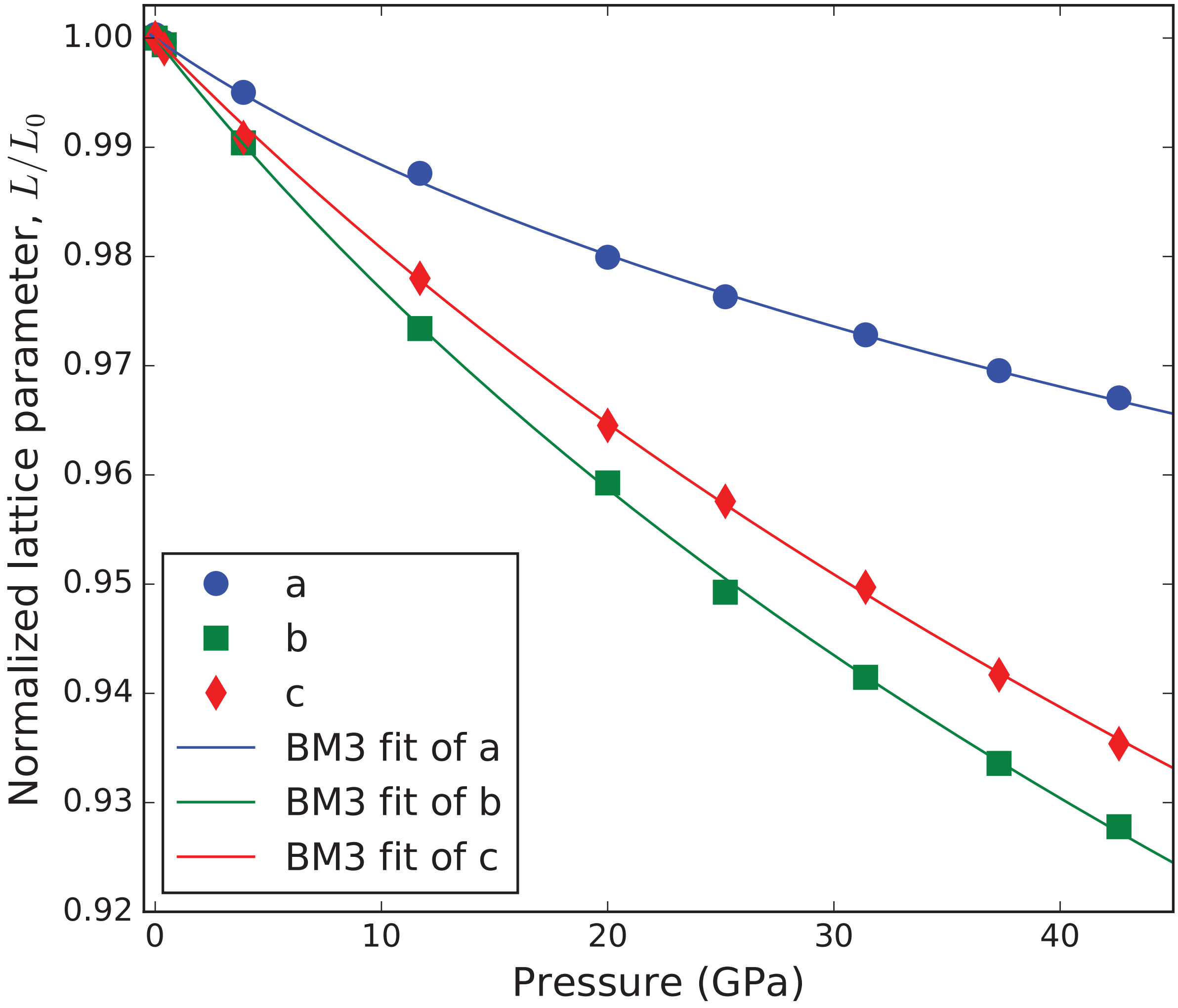
1.00
0.99
0.98
0.97
0.96
0.95
0.94
0.93
0.92
Normalized lattice parameter, L/L_0
0
10
20
30
40
Pressure (GPa)
● a
■ b
♦ c
BM3 fit of a
BM3 fit of b
BM3 fit of c

Figure 3

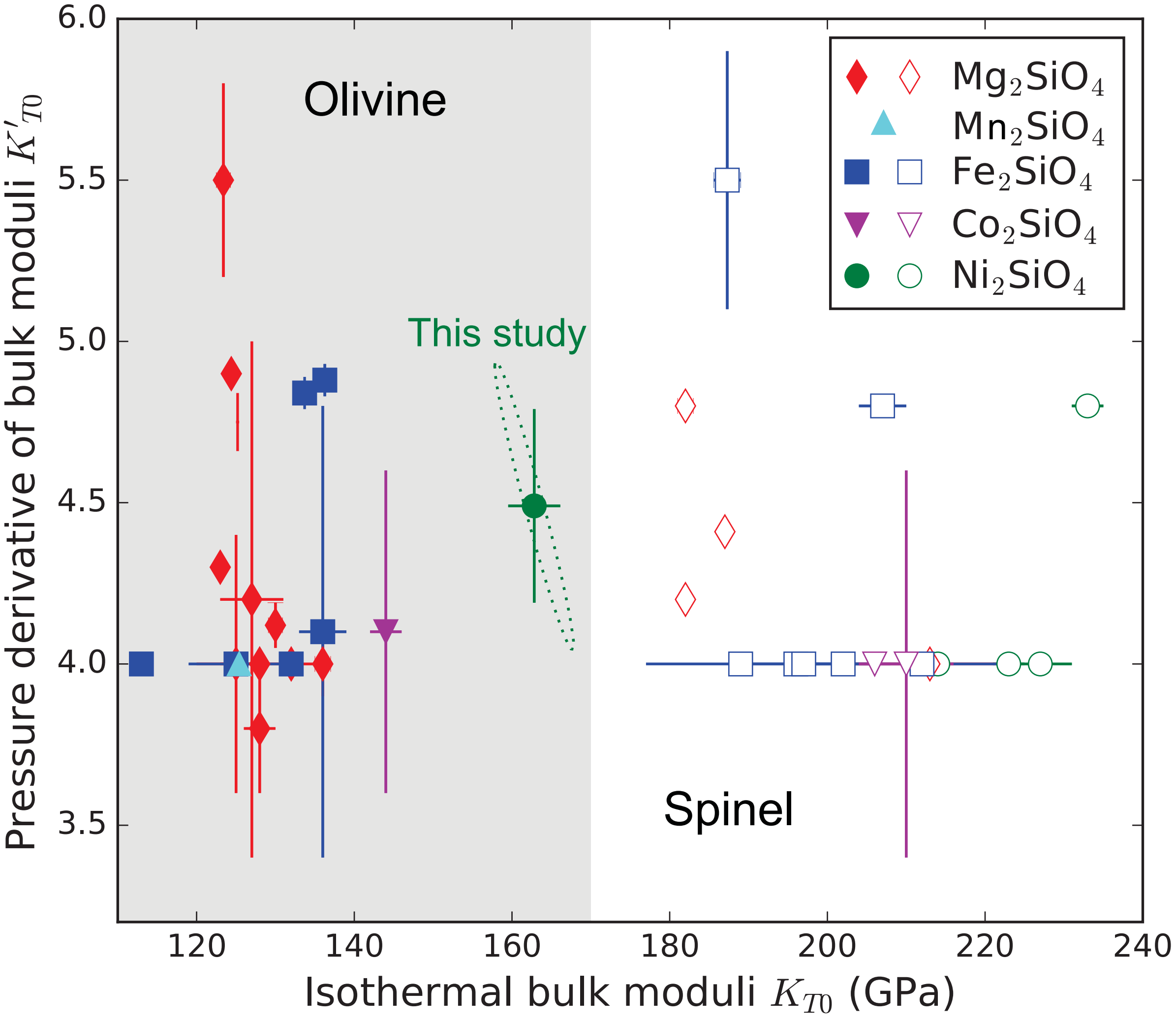
Olivine
Spinel
This study
Mg_2SiO_4
Mn_2SiO_4
Fe_2SiO_4
Co_2SiO_4
Ni_2SiO_4
Pressure derivative of bulk moduli K'_{T0}
Isothermal bulk moduli K_{T0} (GPa)
6.0
5.5
5.0
4.5
4.0
3.5
120
140
160
180
200
220
240

Figure 4

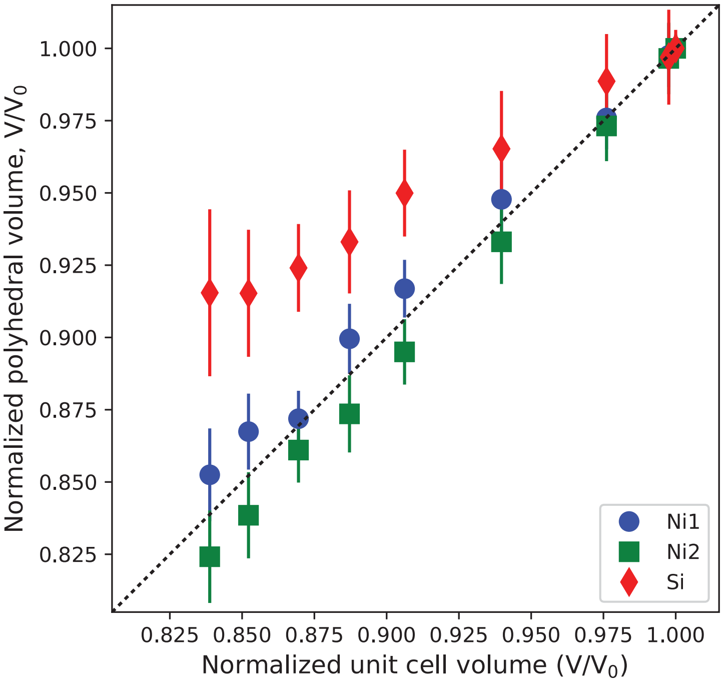
Normalized polyhedral volume, V/V$_0$
1.000
0.975
0.950
0.925
0.900
0.875
0.850
0.825
0.825
0.850
0.875
0.900
0.925
0.950
0.975
1.000
Normalized unit cell volume (V/V$_0$)
Ni1
Ni2
Si

Figure 5

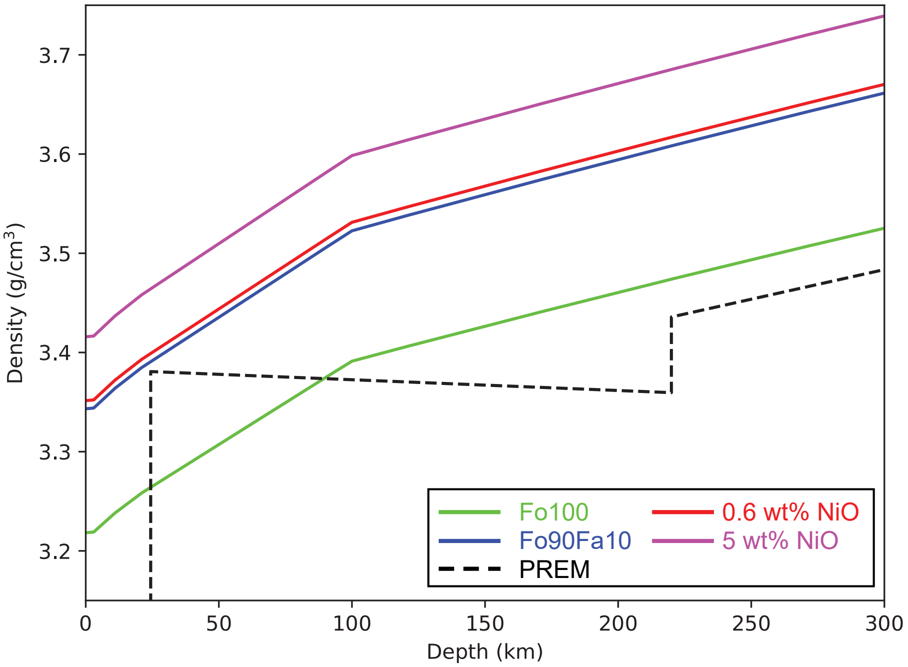
3.7
3.6
3.5
3.4
3.3
3.2
Density (g/cm^3)
0
50
100
150
200
250
300
Depth (km)
Fo100
Fo90Fa10
PREM
0.6 wt% NiO
5 wt% NiO